Numerical investigation on the shear behavior of rock-like materials containing fissure-holes with FEM-CZM method

Wei Han[a], Yujing Jiang[a*], Hengjie Luan[b], Yiteng Du[c], Yinge Zhu[c], Jiankang Liu[a]

[a] Graduate School of Engineering, Nagasaki University, Nagasaki 852-8521, Japan

[b] College of Energy and Mining Engineering, Shandong University of Science and Technology, Qingdao 266590, China

[c] Shandong Provincial Key Laboratory of Civil Engineering Disaster Prevention and Mitigation, Shandong University of Science and Technology, Qingdao 266590, China

Corresponding author: Yujing Jiang

Email: jiang@nagasaki-u.ac.jp

Corresponding Address:

Graduate School of Engineering, Nagasaki University,1-14 Bunkyo-machi, 852-8521 Nagasaki, Japan.

Phone: +81-95-819-2612 Fax: +81-95-819-2627

Numerical investigation on the shear behavior of rock-like materials containing fissure-holes with FEM-CZM method

Abstract: Holes, including their shape and distribution, significantly affect the performance in rocks. In this paper, a numerical investigation, based on a FEM-CZM method, was developed to explore the shear behavior of rock-like materials containing fissure-holes. The laboratory uniaxial compression test was initially performed, and a corresponding numerical model was established by inserting zero-thickness cohesive elements into finite elements globally, the mechanical parameters were acquired by parameter trial and error tests. Subsequently, numerical direct shear tests were conducted under the constant normal stress level. Finally, the mechanical properties, shear deformation, and cracking behaviors were respectively discussed. The results show that for rock-like materials containing fissure-holes, the shearing process can be divided into four typical stages from the perspective of the cohesive elements. In addition, the mechanical characteristics (i.e., peak shear strength, residual shear strength, and crack initiation stress), shear deformation, and cracking behaviors (i.e., crack initiation, propagation, and coalescence), as well as the coalescence mechanism strongly depend on the shape, ligament angle, and the combination of fissure-holes. Furthermore, based on the damaged cohesive elements, the rock bridge coalescence modes between two fissure-holes were identified as DT (dominated by tensile damage), T (tensile damage), and S+T (shear and tensile damage), respectively.

Keywords: Fissure-holes; Cohesive elements; FEM-CZM; Shear behavior; Crack propagation

1. Introduction

Rocks are naturally embedded with a variety of defects [1-3]. The defects, such as fissures, holes, and joints, can be regarded as the dominant factors governing mechanical properties and fracture behavior of rock masses. Generally, such defects can be considered as a source of crack initiation, which in turn propagate and coalesce with other flaws, resulting in the failure of rock masses. Therefore, research on the mechanical characteristics and crack evolution mechanism of rock materials containing flaws is essential to predict geological hazards.

Fractured rock materials primarily contain two groups of flaws, i.e., crack-like flaws and hole-like flaws [4]. Extensive investigations have been conducted for the mechanical behavior and crack growth mechanism on specimens containing crack-like flaws in either rock-like materials or real rocks [5-9]. As for the hole-like flaws, Liu et al. [10] carried out uniaxial compression tests for sandstone specimens containing elliptical holes and fissures to reveal the strength properties and fracture mechanism. In their research, the ligament angle is proved to be a significant factor affecting the strength and crack behaviors. Huang et al. [11] conducted uniaxial compression testes on granite specimens containing three non-coplanar holes, and three typical crack patterns are identified as shear, mixed tensile and shear, and tensile. Yin et al. [12] focused on the effect of hole diameter and temperature levels on the mechanical properties of flawed sandstone specimens containing a single hole under uniaxial compression tests, and the ultimate failure modes were also evaluated. Lajtai et al. [13] conducted polyaxial compression tests to explore the effect of pre-existing openings on the collapse events, and four crack types (i.e., primary tensile, normal shear, secondary tensile and inclined shear fracture) were identified under different confining pressure. Yang et al. [14] performed laboratory experiments on red sandstone containing two oval flaws to explore the crack evolution behavior under uniaxial compression, and they demonstrated that the coplanar flaw angle is a key factor to influence the mechanical behavior. Lin and Wong et al. [15,16] explored the crack coalescence mechanism of granite containing multiple holes loaded in a state of uniaxial compression, various factors such as normalizes bridge, bridge angle, and the number of holes were considered to investigate the change on crack coalescence mechanism. Zhou et al. [4] analyzed the fracture coalescence behavior of marble specimens containing rectangular cavities under uniaxial loading, and four failure modes are observed in specimens, namely splitting failure, shear failure, mixed failure, and surface spalling. Gui et al. [17] paid attention to the effect of opening defects on the mechanical properties and fracture process in rocks under uniaxial loading. It is found that the opening defects, such as their size, shape, distribution, and opening ratio, can significantly influence the rock strength, stiffness, and crack behavior. Yin et al. [18] focused on the effect of pre-existing flaw-hole on the mechanical behavior and crack coalescence modes under uniaxial compression, the effects of fissure angle, ligament length, fissure length and hole diameter on were evaluated.

The finite element method (FEM) has been extensively utilized to explore the mechanical and cracking behaviors of fractured rock masses [19-21], in which the rock materials can be regarded as a continuum. However, some researchers revealed that the rock materials are non-continuum at a microscopic level [22]. Thus, the discrete element method (DEM) was introduced to describe the mechanical properties and cracking behaviors of non-continuum [23-26]. Actually, the rock materials are identified as the combination of a continuum and a non-continuum, the mechanical and fracture behaviors of rock masses could be better presented by the combination of them [27]. The emergence of the cohesive zone model (CZM) combined with FEM was an important step forward to this numerical technique. The work reported here is a numerical work conducted by Jiang et al. [28]. They obtained the micro-parameters of the rock by the numerical model of Brazilian disc and uniaxial compression tests with inserting cohesive elements into finite element, and the 3D rock fracture was subsequently investigated. Chang et al. [29] conducted numerical tests to simulate the complex crack behaviors in layered discs with a pre-existing interface crack based on the CZM method, which was further validated by Brazilian tests. Zhang et al. [30] investigated the shear behavior of jointed rocks by inserting cohesive elements into solid elements, and the crack evolution was concerned in their research. Wang et al. [31] explored the shearing process and failure types of jointed rock masses using the CZM method, and the crack evolution process was further examined.

Note that, for rocks or rock-like materials containing hole-like flaws, most researches concentrated on the mechanical and cracking behaviors under uniaxial compression, whereas information under shearing is rather limited. However, failure caused by the shearing effect can also commonly occur in slopes (see Fig.1 a, b). In addition, the FEM-CZM method could be better to describe the properties of the combination of a continuum and a non-continuum. Unfortunately, fewer appeared in rocks containing discontinuity, and its application should be further discussed and verified. Therefore, the focus of this study is to numerically explore the shear behavior of the rock-like materials containing fissure-holes with a developed FEM-CZM method, and three shapes of fissure-holes (i.e., fissure-circular hole, fissure-elliptical hole, and fissure-square hole) were considered (Fig.1c). This study is expected to improve the understanding of the shear failure mechanism of rock bridges in rock slopes.

2. FEM-CZM method

2.1. Initial liner elastic traction-separation behavior

The traction-separation model available in finite element program Abaqus assumes an initially linear elastic behavior, followed by the initiation and evolution of damage [32,33]. This elastic behavior is defined by an elastic constitutive matrix that describes the nominal stresses to the nominal strains across the interface. The corresponding stress and separation vectors are governed by the following elastic constitutive law:

$$t=\begin{Bmatrix} t_n \\ t_s \\ t_t \end{Bmatrix}=\begin{bmatrix} E_{nn} & E_{ns} & E_{nt} \\ E_{ns} & E_{ss} & E_{st} \\ E_{nt} & E_{st} & E_{tt} \end{bmatrix}\begin{Bmatrix} \varepsilon_n \\ \varepsilon_s \\ \varepsilon_t \end{Bmatrix}=\frac{1}{T_0}\begin{bmatrix} E_{nn} & E_{ns} & E_{nt} \\ E_{ns} & E_{ss} & E_{st} \\ E_{nt} & E_{st} & E_{tt} \end{bmatrix}\begin{Bmatrix} \delta_n \\ \delta_s \\ \delta_t \end{Bmatrix}=\frac{1}{T_0}K\delta \qquad (1)$$

where t is the nominal traction stress vector; t_n is the normal traction, t_s and t_t are the two tangential tractions (shear cohesion); ε_n, ε_s and ε_t are the three components of the nominal strain; T_0 is the initial thickness of the cohesive element, δ is the corresponding displacement component; and K is the stiffness matrix for the cohesive element.

2.2. Damage evolution stage

In the damage evolution stage, which can be shown in Fig.2, normal tractions t_n, and two tangential tractions t_s and t_t would decrease monotonically with the corresponding displacements of the crack surfaces. As these tractions decrease to zero, the cohesive element would be completely damaged, inducing cracks. In our research, mode-I fracture energy $G_{f\mathrm{I}}$ and mode-II fracture energy $G_{f\mathrm{II}}$ were adopted to describe the fracture of rock materials. It should be noted that the fracture energy can be determined by the areas under the corresponding traction curves. Here, initial stiffness (tensile k_{n0} and shear stiffness k_{s0}, k_{t0}), ultimate traction (t_{n0}, t_{s0}, t_{t0}), and the fracture energy (G_{fI}, G_{fII}) were utilized to meticulously investigate the damage process of cohesive elements.

To describe the damage evolution of a crack under a combination of normal and shear deformation on the crack surface, it is necessary and valuable to introduce an effective displacement, as expressed below:

$$\delta_m = \sqrt{<\delta_n>^2 + \delta_s{}^2 + \delta_t^2} \tag{2}$$

where < > is the Macaulay bracket, and it guarantees that damage evolution of cohesive elements will occur only under the action of tension; $<\delta_n>$ is equal to δ_n when δ_n is larger than zero, otherwise, $<\delta_n>$ is equal to zero.

In addition, the damage variable D is introduced to describe the process of damage evolution. As the loading further increases, the value of D evolves from 0 to 1, and the cohesive element reaches its ultimate bearing capacity. The damage variable D can be expressed as follows:

$$D = \frac{\delta_{mf}(\delta_{mm} - \delta_{mo})}{\delta_{mm}(\delta_{mf} - \delta_{mo})} \tag{3}$$

where δ_{mm} is the maximum pure displacement during the loading process; δ_{mo} represents the effective displacement when damage initiates; δ_{mf} is the effective displacement when the tractions diminish.

The normal stress components of the traction-separation model change as follows due to the damage accumulation:

$$t_n = \begin{cases} (1-D)t_{n0}, t_{n0} \geq 0 \\ t_{n0}, \qquad t_{n0} < 0 \end{cases} \tag{4a}$$

$$t_s = (1-D)t_{s0} \tag{4b}$$

$$t_t = (1-D)t_{t0} \tag{4c}$$

Similarly, the tensile and shear stiffness can be described as:

$$k_n = (1-D)k_{n0} \tag{5a}$$

$$k_s = (1-D)k_{s0} \tag{5b}$$

$$k_t = (1-D)k_{t0} \tag{5c}$$

In this paper, the quadratic normal stress criterion was applied to describe the beginning of the stiffness degradation. As a quadratic interaction function involving the normal stress ratios reaches a value of one, the damage initiates. The criterion can be represented as:

$$\left\{\frac{<t_n>}{t_{n0}}\right\}^2 + \left\{\frac{t_s}{t_{s0}}\right\}^2 + \left\{\frac{t_t}{t_{t0}}\right\}^2 = 1 \tag{6}$$

2.3. Insertion of zero-thickness cohesive elements

To accurately reveal the cracking behaviors of rock fracture without a pre-set crack path, cohesive elements should be inserted into the initial finite mesh globally. Note that the cohesive elements should be set to zero-thickness to ensure the insertion of cohesive elements cannot change the original size of the model. The inserting process of cohesive elements can be presented in Fig.3. Firstly, discrete solid elements and read the node information of the entire model into the program (Fig.3a). Secondly, the nodes were re-arranged to realize the nodes of each element do not share with others (Fig.3b). Subsequently, sort the nodes of the cohesive elements, the order of nodes conforms to the right-hand grip rule (Fig.3c). At final, a zero-thickness cohesive element can be generated by outputting the nodes on the coincident surface and assigning a new element number and type (Fig.3d). Due to the tremendous number of solid elements, manually inserting cohesive elements into the interface between the adjacent solid elements is very tedious. Therefore, we developed an internal computer program based on MATLAB to realize the automatic inserting of zero-thickness cohesive elements into solid elements.

3. Model establishment

3.1. Parameters determination

To obtain the mechanical parameters of the rock-like material, the standard cylindrical specimen with dimensions of 100mm length and 50mm diameter was adopted to conduct the uniaxial compression test [34]. The specimen was loaded uniaxially in compression using TAW-1000 electrohydraulic servo-controlled rock mechanics testing apparatus (Fig.4a) at a shortening rate of 0.002mm/s to ensure a static loading condition [34]. Also, a corresponding numerical model was established with inserting zero-thickness cohesive elements into solid elements to acquire the fracture damage parameters, as shown in Fig.4b. Concerning the constitutive model, a linear elastic behavior was adopted for solid elements. Regarding the cohesive elements, a linear softening criterion was selected to describe the damage evolution. Additionally, an ideal elastoplastic model was chosen for the steel plate. For the boundary conditions, the bottom of the steel plate is fixed along the vertical direction, while a constant loading rate is applied on the top boundary. Theoretically, the loading rate used in the simulation should be the same as the one used in the experiment. However, the low loading rate will result in an enormous number of steps. Thus, the loading rate in the simulations is 0.1mm/s. With respect to the mesh quality, 77978 number of zero-thickness cohesive elements (COH3D6) were inserted into the 43155 number of solid elements (C3D4) globally in 36s with the self-developed program. The approximate failure pattern and mechanical behavior can be acquired by a series of parameter trial and error tests.

A comparison of the experimental and numerical results in the uniaxial compression test can be presented in Fig.5, which illustrated that they are very consistent. The numerical and experimental peak compressive stress of approximately 45MPa both occur near an axial strain of 0.42%, and their post-peak curves exhibit similar trends. Meanwhile, the comparison of the fracture patterns in the numerical and experimental was also shown in Fig.5, both show a similar main diagonal split tensile fracture pattern. In addition, the fracture process under different steps of the specimen is presented in Fig.6. It is observed that the damaged cohesive elements appear first in the middle of the specimen. As the calculated step increases, the failure part will graduate expand along the diagonal direction, causing tensile fracture failure from inside to outside.

In this paper, both the failure mode and the mechanical properties of the numerical simulation are highly consistent with the experimental. In addition, the fracture process of the specimen in the numerical model can also well explain the failure features. Therefore, the mechanical parameters acquired in the numerical can be utilized to explore the shear behavior of rock-like materials, and the numerical parameters are listed in Table 1.

3.2. Model establishment for the direct shear test

A conceptual model for rock-like materials containing fissure-holes is presented in Fig.7. Regarding the size adopted in this paper, it should be indicated that the collisions and misalignments occur between solid elements when the rock mass ruptures, the global contact, therefore, was used to define the contact behavior. Although the influence of the direction perpendicular to the loading plane on the shear behavior is negligible, the global contact can only be applied to 3D surface contact. Further, the length and height of the specimen were determined by the standard laboratory direct shear tests [35]. Thus, the rock-like specimens in this paper for direct shear tests were arranged 3D model with a size of length 200mm× wide 1mm×height 100mm. For the boundary conditions, the upper surface is loaded by constant normal stress, the bottom and the right-lower boundary are constrained completely. The shearing direction arises from left to right with a constant loading velocity. In this paper, three shapes of holes were considered, respectively elliptical hole, circular hole, and square hole. Their geometries are defined as follows: the length of the major ellipse axis a, the length of the minor ellipse axis b, the radius of the circular hole R, the length of the square hole c, the ligament angle α (the angle between fissure and horizontal axis), and the opening area of the two holes S. Furthermore, the length of the edge-notched flaw and fissure in holes are respectively set to 20mm and 10mm. The detailed schematics of fissure-holes in the numerical model are presented in table 2. Notably, the opening area of each specimen remains the same to eliminate the effect of the opening rate (area of opening/specimen area).

4. Numerical results

4.1. Mechanical properties

The shearing process of rock-like materials containing fissure-holes of cases AI-AIII can be illustrated in Fig.8. It is observed from Fig.8a that the shear stress-shear displacement curves exhibit similar characteristics. Specifically, the shear stress gradually increases to its peak with a slight decrease during the growth process. Subsequently, the shear stress shows a decreased trend, but there exists a slight increase during the decline. At final, the shear stress reaches the residual stage, remaining small fluctuations. Note that the shearing process of rock-like materials containing fissure-holes can generally be divided into four typical stages (I-IV). At stage I, the shear stress approximately linearly increases with increasing the shear displacement, which can be regarded as the elastic strengthening phase. In this stage, as shown in A of Fig.8b, all solid and cohesive elements maintain a complete connection without any crack initiation, and none of the cohesive elements reaches the initial damage stress and fracture toughness. As the shear displacement increases, the shearing process will enter the crack strengthening phase (Stage II). In this stage (B and C), some cohesive elements near flaw tips will first enter the failure state, inducing cracks (crack initiation is at the junction of stage I and stage II). The cohesive elements at the crack suffered irreversible damage, causing a small decrease in local shear strength. However, the local cracks and the decrease in stiffness will cause the main load-bearing objects to be transferred to other parts, resulting in a more uniform distribution of stress, the shear strength, therefore, can be increased further. With the further increase of the shear displacement, the shearing process will enter the plastic softening phase (Stage III). At this stage (D), a large number of cohesive elements failed, leading to a rapid increase in the number of cracks. Meanwhile, the shear strength and shear stiffness decrease significantly, inducing local instability. According to stage IV, the rock bridge coalescence cracks occur, and the specimen enters the stage of residual strength. In this stage, cohesive elements failed along the rock bridge coalescence path, causing the specimen to be completely destroyed (E). It should be indicated that the residual shear strength is mainly provided by the mechanical occlusion and friction between the solid elements. Notably, the shearing process is strongly affected by the shape of fissure-hole. More specifically, when the rock-like material contains fissure-circular holes, the stage of elastic strengthening is larger than that of other shapes. That is because the distribution of stress is relatively uniform, and a slightly larger shear displacement is required to induce cracks. Moreover, when the rock-like material contains fissure-elliptical holes, the plastic soften stage is larger than that of other shapes, indicating that relatively good ductility is formed.

Fig.9 displays the peak shear strength, residual shear strength, and crack initiation stress in rock-like materials containing fissure-holes. According to Fig.9a, the value of peak shear strength for the fissure-elliptical hole is 13.9

MPa, which is decreased by 7.9% and 6.8% respectively compared with fissure-circular and square holes, indicating that the rock-like materials containing fissure-elliptical holes have a weaker ability to withstand shearing effect than that of other shapes. Analogously, the value of residual shear strength for the fissure-elliptical hole is 3.2 MPa, which is also less than that of other shapes. However, concerning the crack initiation stress, the value of fissure-square hole is 5.3 MPa, which is smaller than the fissure-elliptical hole (6.1 MPa) and fissure-circular hole (5.7 MPa), indicating that crack initiation of rock-like materials containing fissure-square holes most easily occurs, which is caused by the wide distribution of the tips in the square hole. The fissure-elliptical holes were selected with different ligament angles (0°, 60°, and 90°, respectively) to determine its effect on mechanical properties (Fig.9b). When the ligament angle is 90°, the peak shear strength and residual shear strength are 13.9 MPa and 7.5 MPa, respectively, which are larger than that of 0° and 60°. Note that the value of peak shear strength of ligament angles at 0° is the smallest (13.1 MPa), denoting that the rock-like materials containing fissure-holes with ligament angles of 0° have a weaker ability to withstand shearing effect than that of other ligament angles. Similarly, the crack initiation stress presents the same characteristics as the peak shear strength, which implies that cracks most easily occur with the ligament angle of 0° for fissure-holes. As shown in Fig.9c, the fissures-holes were arranged with three types of combinations to investigate their mechanical behaviors. Concerning the peak shear strength, the combination of a fissure-square hole and a fissure-elliptical hole is 13.9 MPa, which is smaller than that of other combinations. Whereas for the residual shear strength, the combination of a fissure-square hole and a fissure-circular hole is the largest (6.4 MPa). Additionally, regarding the crack initiation stress, the values of the three combinations are 5.14 MPa, 5.13 MPa, and 5.11 MPa, respectively. It can be observed that the difference is not obvious, which indicates that crack initiation occurs almost simultaneously.

The relation of shear stress and shear displacement under different loading conditions can be shown in Fig.10. Taking the fissure-square hole as an example, the shear stress-shear displacement curves for rock-like materials under different shear rates (i.e., 0.01mm/s, 0.02mm/s and 0.05mm/s) are illustrated in Fig.10a. Note that the peak shear strength, residual shear strength, and crack initiation stress all increase with the increment of shear rate. Additionally, with respect to the shearing process, when the shear rate is large, the elastic strengthening phase shrinks, while the crack strengthening phase prolongs. In other words, the greater the shear rate, the easier the crack will be generated. That is because when the shear rate is large, the cohesive elements will first reach the initial damage stress and fracture toughness due to the large concentrated traction force, resulting in a small elastic strengthening phase and a large crack strengthening phase. Furthermore, the larger the shear rate, the shorter the plastic soften stage, inducing a larger brittleness. In accordance with Fig.10b, the shear stress-shear displacement curves are also strongly influenced by applied constant normal stress levels. It is apparent that the peak shear strength, residual shear strength, and crack initiation stress evolve with applied normal stress exhibit a similar trend with the shear rates. Moreover, note that enlarging the applied normal stress does not significantly affect the shearing process.

4.2. Vertical deformation characteristics

The vertical deformation of the specimen during the direct shear process can reflect its dilatancy characteristics. The distribution of vertical displacement evolves with shear displacement is shown in Fig.11. It should be pointed out that the specimen is in a shear shrinkage when the value of vertical deformation is negative, while a positive value denotes the state of shear dilatancy. As plotted in Fig.11a, note that the specimen is in a compressed state when the shear displacement is 0, which is caused by the applied constant normal stress. With the increase of shear displacement, the specimen gradually changes from the state of shear shrinkage to dilatancy, which is due to the collisions and misalignments between solid elements during the shearing process. In addition, the maximum shear dilatancy is affected by the shape of fissure-hole obviously. Specifically, for fissure-circular holes, the maximum shear dilatancy is 1.46mm, while 1.44mm and 0.9mm for fissure-square holes and fissure-elliptical holes, respectively. As seen from Fig.11b. the maximum shear dilatancy is 1.78mm when the ligament angle is 90°, which is larger than that of 0° and 60°. That is because the vertical opening size is large along the direction of applied normal stress when the ligament angle is 90° . Fig.11c presents the curves of vertical deformation-shear displacement for the specimen with different combinations of fissure-holes. Note that the combination of fissure-square hole and fissure-circular hole exhibits larger shear dilatancy than that of other combinations. In addition, for the combination of fissure-square hole and fissure-elliptical hole, the peak shear dilatancy occurs when the shear displacement is 1.02mm, which is smaller than that of other combinations. Moreover, after the peak of shear dilatancy, there is still a small fluctuation, which is caused by the collisions between the solid elements.

Fig.12 displays the relation of vertical deformation and shear displacement under different loading conditions. According to Fig.12a, the maximum shear dilatancy displays a positive correlation with the shear rate obviously. Specifically, as the shear rate increase to 0.02mm/s and 0.05mm/s, the maximum shear dilatancy becomes 1.4 mm and 1.7 mm, respectively. This is because when the shear rate is large, the transposition between the solid elements is intensified, and there is not enough time to rearrange, resulting in a large expansion. In addition, it is observed that the shear displacement corresponding to the maximum dilatancy displays an increasing trend with the shear rate. Fig.12b displays the relation between the vertical displacement and shear displacement under different applied normal stress levels. Note that when the applied normal stress is 1MPa, the maximum shear dilatancy is 2.3mm. As the applied normal stress increases to 1.5MPa and 2MPa, the maximum dilatancy becomes 1.51 mm and 0.92 mm, respectively. In other words, the larger the applied normal stress is, the smaller the shear dilatancy is. That can be explained by the restraint effect applied on the specimen in the normal direction, the smaller the applied normal stress is, the less the restraint effect is, inducing larger shear dilatancy. Moreover, it is apparent that the shear displacement corresponding to the maximum shear dilatancy is almost the same under different normal stresses, which indicates that the transposition between the solid elements hardly affected by applied normal stress.

4.3. Description of cracking behavior

4.3.1. Effect of shape of fissure-holes

In this section, the stress distribution along the shear direction and the fracture process patterns of cases AI-AIII are gathered and presented in Fig.13. By observing the crack initiation, note that the initiation of crack all starts from the right-bottom tip of the left edge-notched flaw with different initiation angle β. Specifically, for fissure-circular holes, the crack initiation angle is 135°, while for fissure-square and elliptical holes, the β is 60° and 120°, respectively. As can be seen from the stress distribution, the tension stress zone is distributed in the right-upper sides of the left edge-notched flaw, while the compression zone for the left-bottom sides of the left edge-notched flaw. It can be concluded that tensile fracture is a dominant mode of failure for crack initiation. According to the crack propagation, note that the order of cracks appears and where they initiate as well as the paths of crack propagation morphology are basically the same with the exception of crack 2. As for the fissure-circular holes, the crack 2 emanates from the left-upper tip of the left fissure-circular hole. However, for the fissure-square and elliptical holes, crack 2 all initiates from the holes. That is because the stress distribution around the hole is affected by the shape of the hole. In other words, the curvature of the circular hole is smaller than that of the elliptical hole, the stress distribution around the circular hole is much more uniform. Thus, cracks are more prone to occur near the elliptical hole than the circular hole, whereas for square holes, the stress concentration is formed due to the existence of tips, inducing cracks near the square hole more easily. As the shear displacement increases, the generated cracks continue to expand, intersect, and then the specimen enters the crack coalescence stage. It is observed that the mode of crack coalescence is sensitive to the shape of fissure-holes. Specifically, the rock bridge coalescence patterns between the two fissure-circular holes are mainly linked by the fissures. Whereas for the fissure-square or square hole, the coalescence paths are composed of two parts, connected by fissure to hole or fissure to fissure, respectively. In addition, there are other cracks initiating randomly across the whole specimen, those are connected to the main cracks and run through the specimen, causing the complete failure. Moreover, the phenomenon of spalling (failure caused by the coalescence of cracks) generally occurs along the main shear sliding paths.

To explore the crack coalescence mechanism, it is necessary to identify the type of generated cracks according to the damaged cohesive elements. The MMIXDME, which represents the proportion of fracture modes during damage evolution, was utilized to determine the damage type of cohesive elements. Specifically, when the value of MMIXDME is in the range of 0 to 0.5, the cohesive elements are dominated by tensile damage, resulting in tensile cracks, while controlled by shear damage (shear cracks) when the value is in the range of 0.5 to 1. In addition, when the value is equal to -1, the cohesive elements are not damaged at this time. Here, taking case AIII as an example, the failure mode based on the cohesive elements can be illustrated in Fig.14a. According to the judge criteria indicated above, the types of coalescence cracks are displayed in Fig.14b. Note that the rock bridge between the left edge-notched flaw and the left fissure-elliptical hole coalesces in the form of shear cracks along the lower path, while tensile cracks in the upper path. In addition, the rock bridge coalescence between the two fissure-elliptical holes is dominated by tensile cracks, but with local shear cracks. Furthermore, the two coalescence paths are formed between the right fissure-elliptical hole and the right edge-notched flaw, the propagation of shear cracks along the upper path leads to shear crack coalescence, while the tensile cracks along the lower path.

Fig.15 illustrates the coalescence cracks pattern of rock-like materials containing fissure-circular and fissure-square holes. It is observed that the two rock bridge coalescence paths between the left edge-notched flaw and the left fissure-circular hole are caused by mixed shear-tensile cracks. While for the fissure-square holes, the cohesive elements along the upper coalescence path are dominated by shear damage, but tensile damage along the lower path. For the fracture pattern of rock bridge between the right edge-notched flaw and the right fissure-hole, the coalescence path is caused by tensile cracks for the fissure-circular hole, while shear cracks for the fissure-square hole. Similarly, the rock bridges between the two fissure-holes are all mainly ruptured by the expansion of tensile cracks, propagating following the approximate straight path. It is also noted that shear cracks connected with holes are distributed along the circular hole in the form of approximately center symmetry. Overall, for fissure-circular holes, the fractures exhibit the characteristics of interval distribution of shear and tensile cracks along the path of coalescence cracks. Concerning the fracture pattern for fissure-square holes, the left and right rock bridges are mainly ruptured by shear damage, while the rock bridge between the two fissure-square holes is dominated by tensile damage. Therefore, the damage types of coalescence are strongly dependent on the shapes of the fissure-holes.

4.3.2. Effect of ligament angle of fissure-holes

The stress distribution along the shear direction and the fracture process patterns of specimen containing fissures-elliptical holes with different ligament angles (i.e., 0°, 90°) are displayed as Fig. 16. Regarding the crack initiation, all emanate from the tip of the left edge-notched flaw with different crack initiation angle β. Specifically, when the ligament angle is 90°, the β is equal to 60°, while for the ligament angle of 0°, the β is equal to 120°. In addition, note that the crack initiation is also caused by the tensile effect. With the shear displacement increment, new cracks are continuously generated in sequence. It is observed that during the crack propagation stage, the cracks appear in roughly the same order except for crack 6 and 7. When the ligament angle is 90°, the crack 6 appears at the left upper tip of the right edge-notched flaw, whereas for the ligament angle is 0°, the crack 6 arises from the left edge-notched flaw. As generated cracks continue to propagate and intersect, the specimen enters the crack coalescence stage. It is observed that the coalescence patterns strongly depend on the ligament angle of fissure-holes. Specifically, the left rock bridge is penetrated by three coalescence paths when the ligament angle is 90°, but two coalescence paths when the ligament angle of 0°. For the middle rock bridge, two main coalescence paths generated when the ligament angle is 90°, whereas only one coalescence path appeared when the ligament angle of 0°. Note that, the coalescence paths of the right rock bridge generally occur in the lower zone when the ligament angle is 90°, while in the upper zone for that of 0°. Furthermore, large-scale spalling is observed along the coalescence path when the ligament angle is 90°, while for the ligament angle of 0°, the spalling phenomenon generally forms at both edges of the specimen.

To determine the coalescence mechanism of rock-like materials containing fissure-elliptical holes with different ligament angle, the damaged types of coalescence cracks were gathered according to the cohesive elements, as shown in Fig.17. It can be seen from Fig.17a that the three rock bridge coalescence paths between the left edge-notched flaw and the left fissure-elliptical hole are caused by shear cracks, mixed shear-tensile cracks, and tensile cracks, respectively. However, only shear crack coalescence is responsible for the breakage of the left rock bridge when the ligament angle is 0° (Fig.17b). In addition, the rock bridge coalescence between the two elliptical holes is mainly ruptured by the expansion of tensile cracks when the ligament angle is 0°. While for the ligament angle of 90°, the middle rock bridge coalesced in the form of tensile, tensile, shear, and shear damage, respectively. With respect to the right rock bridge, the damaged cohesive elements along the coalescence paths are all mainly caused by mixed tensile-shear damage.

4.3.3. Effect of combination of fissures-holes

The stress distribution along the shear direction and the fracture process patterns of the specimen containing different combinations of fissures-holes are displayed in Fig. 18. Concerning the initiation of crack, all emanate from the tip of the left edge-notched flaw with different crack initiation angle β (60° for case CI, 120° for case CII, and 130° for case CIII, respectively). In addition, the tensile fracture is also a dominant mode of failure for crack initiation. According to the crack propagation, note that the patterns are roughly similar except for crack 4 and 5, which can be observed from case CI and CII (the right fissure-elliptical hole is changed to fissure-circular hole). Specifically, crack 4 appears at the upper fissure of the right fissure-elliptical hole for CI, while for case CII, the crack 4 arises from the lower fissure of the right fissure-circular hole. By comparing case CI with CIII (the left fissure-square hole is changed to fissure-circular hole), note that the initiation position of crack 2 is different. More specifically, the crack 2 starts from the square hole in case CI, whereas in case of CIII, the crack 2 emanates from the fissure of the left fissure-circular hole, which demonstrates again that the shape of holes can affect the stress distribution. As generated cracks continue to propagate and intersect, the specimen enters the crack coalescence stage, as shown in Fig.18. According to the coalescence cracks pattern in the left rock bridge, there are two, three, and three coalescence paths in CI, CII, and CIII, respectively. It should be indicated that between the two fissure-holes, the main coalescence paths are generated in an oblique direction for case CI. In contrast, the two main coalescence paths are parallel for case CII, but only one path appears and is connected by two fissures for case CIII. Moreover, the spalling phenomenon is liable to occur near the holes for case CII, while for case CI and CIII, the spalling zone is prone to be generated near the fissures.

The damaged types of coalescence cracks are identified according to the cohesive elements, as shown in Fig.19. It can be seen from the comparison of case CI and CII (Fig.19 a, b), the upper coalescence paths of left rock bridge are all caused by shear cracks, but tensile cracks in the lower paths. Concerning the rock bridge between the two fissure-holes, the cohesive elements along the coalescence paths are dominated by mixed shear-tensile damage for case CI, while dominated by tensile damage for case CII. On the other hand, when the left fissure-square hole is changed to the fissure-circular hole, the comparison can be indicated in Fig.19 a, c. For case CIII, the tensile crack 1 emanates from the tip of the left edge-notched fissure, extending to not only the left fissure but also the circular hole, forming local tensile failure path, which is different from the case CI. The other difference is that the rock bridge coalescences between the two fissure-holes are dominated by tensile cracks for case CIII. Furthermore, tensile cracks are prone to occur near the left circular hole, while shear cracks for the square hole in case CI. Moreover, the shear damage is prone to occur at the bottom zone of the elliptical hole in case CI, while it appears at the upper area in case CIII.

In general, for case CI, the overall rock bridge coalescence cracks are dominated by shear cracks, but with local tensile cracks between the two fissure-holes. Regarding case CII, the cohesive elements along the coalescence cracks are dominated by tensile damage, but with local shear damage in the left rock bridge. Concerning case CIII, the coalescence cracks are dominated by shear cracks at the two sides of rock bridges, while tensile cracks for the rock bridge between the two fissure-holes. Therefore, it is apparent that the fracture mechanism strongly depends on the distribution and shape of the holes.

4.3.4. Discussion

In this section, the rock bridge coalescence cracks between two fissure-holes are concluded, which can be listed in Table 3. It is observed that three types of coalescence modes can be identified, namely “DT” “T” “S+T”. Meantime, the detailed descriptions of each mode are also presented. Furthermore, in each image of the coalescence pattern, crack junctions are marked as points that need to be focused on in Engineering practice.

5. Conclusions

A comprehensive investigation on the shear behavior of rock-like materials containing fissure-holes was performed with the FEM-CZM method. In the numerical technique, all the initial finite meshes were discretized using zero-thickness cohesive elements globally, which can help to describe the properties of the combination of continuum and non-continuum. Based on this method, the main conclusions can be drawn as follows:

(1) Evolution properties of the shearing process for rock-like materials containing fissure-holes were

investigated and first reported from the perspective of the cohesive elements. Generally, the shearing process can be divided into four typical stages, respectively elastic strengthening stage, crack strengthening stage, plastic softening, and residual strength stage. Note that the crack initiation is at the beginning of the crack strengthening stage. In addition, the shear rate affects the shearing process apparently, i.e. the greater the shear rate is, the shorter the plastic soften stage is, and the larger the brittleness is. However, the applied normal stress hardly affects the shearing process.

(2) The shape and the ligament angle of fissure-holes significantly affect the mechanical properties (i.e., peak shear strength, residual shear strength, and crack initiation stress). The rock-like materials containing fissure-elliptical holes with the ligament angles of 0° has the smallest shear strength. Thus, that should be the focus of reinforcement. In addition, the crack initiation stress in the fissure-square holes is the smallest, which indicates that cracks are more prone to occur than that of other shapes. Therefore, that should be an early concern in fracture engineering.

(3) The shear dilatancy of rock-like materials containing fissure-holes is influenced by the shape and the ligament angle of fissure-holes as well as loading conditions obviously. The maximum shear dilatancy occurred when the specimen contains fissure-elliptical holes with the ligament angle of 90°. In addition, the larger the shear rate is, the greater the maximum shear dilatancy is, the less the applied normal stress is, the larger the maximum shear dilatancy is.

(4) Cracking behaviors, including their initiation, propagation, and coalescence, were analyzed detailed and found that they strongly depend on the shapes, ligament angles as well as the combinations of fissure-holes significantly. In addition, the type of each crack was precisely obtained with the damaged cohesive elements. Furthermore, three types of rock bridge coalescence modes between two fissure-holes can be identified from the point of the failure patterns, namely DT, T, and S+T.

Acknowledgements

This research was funded by Shandong Provincial Natural Science Foundation, China (Grant No. ZR2019BEE065).

Conflicts of interest

The authors declare no conflict of interest.

References

[1] Asadizadeh M, Hossaini MF, Moosavi, M, Masoumi H, Ranjith PG. Mechanical characterisation of jointed rock-like material with non-persistent rough joints subjected to uniaxial compression. Eng Geol 2019; 260

[2] Mondal S, Olsen-Kettle L, Gross L. Simulating damage evolution and fracture propagation in sandstone containing a preexisting 3-D surface flaw under uniaxial compression. Int J Numer Anal Met 2019; 43(7), 1448-66.

[3] Prudencio M, Van Sint Jan M. Strength and failure modes of rock mass models with non-persistent joints. Int J Rock Mech Min Sci 2007; 44 (6): 890-902.

[4] Zhou Z, Tan L, Cao W, Zhou Z, Cai X. Fracture evolution and failure behaviour of marble specimens containing rectangular cavities under uniaxial loading. Eng Fract Mech 2017; 184:183-201.

[5] Zhang, K, Chen, Y, Fan, W et al. Influence of intermittent artificial crack density on shear fracturing and fractal behavior of rock bridges: Experimental and Numerical Studies. Rock Mech Rock Eng 2020; 53, 553-68.

[6] Yang X, Qiao W, Numerical investigation of the shear behavior of granite materials containing discontinuous joints by utilizing the flat-joint model. Comput Geotech 2018; 104:69-80.

[7] Ghazvinian A, Sarfarazi V, Schubert W, Blumel MA. Study of the failure mechanism of planar non-persistent open joints using PFC2D. Rock Mech Rock Eng 2012; 45(5):677-93.

[8] Huang D, Gu DM, Yang C, Huang RQ, Fu GY. Investigation on mechanical behaviors of sandstone with two preexisting flaws under triaxial compression. Rock Mech Rock Eng 2016; 49(2):375-99.

[9] Zhang XP, Zhang Q, Wu S. Acoustic emission characteristics of the rock-like material containing a single flaw under different compressive loading rates. Computers and Geotechnics. 2017; 83:83-97.

[10] Liu XR, Yang SQ, Huang YH, Cheng JL. Experimental study on the strength and fracture mechanism of sandstone containing elliptical holes and fissures under uniaxial compression. Eng Fract Mech 2019; 205:205-17.

[11] Huang YH, Yang SQ, Ranjith PG, Zhao J. Strength failure behavior and crack evolution mechanism of granite containing pre-existing non-coplanar holes: experimental study and particle flow modeling. Comput Geotech 2017; 88:182-98.

[12] Yin Q, Jing HW, Ma GW. Experimental study on mechanical properties of sandstone specimens containing a single hole after high-temperature exposure. Geotech Lett 2015; 5:43-8.

[13] Lajtai E, Lajtai V. The collapse of cavities. Int J Rock Mech Min Sci Geomech Abstr 1975; 12(1):81-6.

[14] Yang SQ, Huang YH, Tian WL, Zhu JB. An experimental investigation on strength, deformation and crack evolution behavior of sandstone containing two oval flaws under uniaxial compression. Engineering Geology 2017; 217:35-48.

[15] Lin P, Wong RHC, Tang CA. Experimental study of coalescence mechanisms and failure under uniaxial compression of granite containing multiple holes. Int J Rock Mech Min Sci 2015; 77:313-27.

[16] Wong RHC, Lin P. Numerical study of stress distribution and crack coalescence mechanisms of a solid containing multiple holes. Int J Rock Mech Min Sci 2015; 79:41-54.

[17] Gui YL, Zhao ZY, Zhang C, Ma SQ. Numerical investigation of the opening effect on the mechanical behaviours in rocks under uniaxial loading using hybrid continuum-discrete element method. Comput

Geotech 2017; 90:55-72.
[18] Yin Q, Jing HW, Su HJ. Investigation on mechanical behavior and crack coalescence of sandstone specimens containing fissure-hole combined flaws under uniaxial compression. Geosciences Journal. 2018; 5(22): 825-42.
[19] Wang SY, Sloan SW, Tang CA. Numerical simulation of the failure mechanism of circular tunnels in transversely isotropic rock masses. Tunn Undergr Sp Tech 2012; 32: 231-44.
[20] Li ZC, Li LC, Li M, et al. A numerical investigation on the effects of rock brittleness on the hydraulic fractures in the shale reservoir. J Nat Gas Sci Eng 2018; 50: 22-32.
[21] Li G, Cheng XF, Pu H, Tang CA. Damage smear method for rock failure process analysis. Journal of Rock Mechanics and Geotechnical Engineering. 2014; 2:1151-65.
[22] Zhu JB, Zhou T, Liao ZY, Sun L, Li XB, Chen R. Replication of internal defects and investigation of mechanical and fracture behaviour of rock using 3D printing and 3D numerical methods in combination with X-ray computerized tomography. Int J Rock Mech Min Sci 2018; 106: 198-212.
[23] Ding XB, Zhang LY. A new contact model to improve the simulated ratio of unconfined compressive strength to tensile strength in bonded particle models. Int J Rock Mech Min Sci 2014; 69: 111-9.
[24] Cao RH, Cao P, Lin H. Peng CZ, Ou K. Mechanical behavior of brittle rock-like specimens with pre-existing fissures under uniaxial loading: experimental studies and particle mechanics approach. Rock Mech Rock Eng 2016; 49: 763-83.
[25] Wong LNY, Zhang XP. Size effects on cracking behavior of flaw-containing specimens under compressive loading. Rock Mech Rock Eng 2014; 47(5):1921-30.
[26] Jiang YJ, Yan P, Wang YH, Luan HJ, Chen YQ. Numerical investigations on shear behavior and failure mechanism of non-persistent jointed rocks. Geotech Geol Eng 2020; 38:1639-51.
[27] Fan LF, Wu ZJ, Wan Z, Gao JW. Experimental investigation of thermal effects on dynamic behavior of granite. Appl Therm Eng 2017; 125: 94-103.
[28] Jiang HX, Meng DG. 3D numerical modelling of rock fracture with a hybrid finite and cohesive element method. Eng Fract Mech 2018; 199: 280-93.
[29] Chang X, Guo TF, Zhang S. Cracking behaviours of layered specimen with an interface crack in Brazilian tests. Eng Fract Mech 2020; 228: 106904.
[30] Zhang SB, Wang G, Jiang YJ, Wu XL, Li GX, He P, Yu JH, Sun LL. Study on shear mechanism of bolted jointed rocks: experiments and CZM-based FEM simulations. Appl Sci 2020; 10 (62):1-21.
[31] Wang G, Zhang SB, Lian L, Zhao C, Wang K, Zhang XD. Macro-micro study on shear failure mechanism of rock joint based on zero-thickness cohesive element. Chinese Journal of Geotechnical Engineering 2019; 41(12): 2224-32.

[32] Xie D, Waas AM. Discrete cohesive zone model for mixed-mode fracture using finite element analysis. Eng Fract Mech 2006; 73(13):1783-96.

[33] Yao Y. Linear elastic and cohesive fracture analysis to model hydraulic fracture in brittle and ductile rocks. Rock Mech Rock Eng 2012; 45:375-87.

[34] Bobet A, Einstein HH. Fracture coalescence in rock-type materials under uniaxial and biaxial compression. Int J Rock Mech Min Sci 1998; 35(7):863-88.

[35] Wang G, Zhang YZ, Jiang YJ, Liu PX, Guo YS, Liu JK, Ma M, Wang K, Wang SG. Shear behaviour and acoustic emission characteristics of bolted rock joints with different roughnesses. Rock Mech Rock Eng 2018; 51(6), 1885-906.

Table Captions

Table 1 Parameters applied in the simulations.

Table 2 Schematics of fissure-holes in the numerical model.

Table 3 Coalescence modes of rock bridge between two fissure-holes.

Figure Captions

Fig.1. Rock mass high slopes: (a) potential sliding path of rock mass containing fissure-holes (Chongqing, China); (b) detailed descriptions of fissure-holes; (c) shapes of fissure-holes considered in this paper.

Fig. 2. Mixed-mode traction-separation response.

Fig. 3. Inserting a zero-thickness cohesive element between solid elements: (a) two adjacent solid elements; (b) re-arranged nodes of solid elements; (c) zero-thickness cohesive element (COH3D6); (d) insertion of a cohesive element.

Fig. 4. Uniaxial compression test: (a) Laboratory test; (b) numerical model.

Fig. 5. Comparison of experimental and numerical results in the uniaxial compression test.

Fig. 6. Fracture process of the specimen under different steps.

Fig. 7. A conceptual model for rock-like materials containing fissure-holes under the shearing effect.

Fig. 8. Shearing process of rock-like materials containing fissure-hole flaws: (a) shear stress-shear displacement curves under different shapes of fissure-holes; (b) characteristics of cohesive elements.

Fig. 9. Mechanical properties (i.e., peak shear strength, residual shear strength, and crack initiation stress) of rock-like materials containing fissure-holes: (a) different shapes of fissure-holes; (b) different ligament angles of fissure-holes; (c) different combinations of fissure-holes.

Fig. 10. Curves of shear stress-shear displacement under different loading conditions: (a) different shear rates; (b) different applied normal stress levels.

Fig. 11. Curves of vertical deformation-shear displacement: (a) different shapes of fissure-holes; (b) different ligament angles of fissure-holes; (c) different combinations of fissure-holes.

Fig.12. Curves of vertical deformation-shear displacement of rock-like materials containing fissure-holes under different loading conditions: (a) different shear rates; (b) different applied normal stress levels.

Fig. 13. Stress distribution and crack growth process in rock-like materials containing different shapes of fissure-hole (i.e., fissure-circular holes, fissure-square holes, and fissure-elliptical holes).

Fig. 14. Shear failure pattern: (a) types of damaged cohesive elements; (b) coalescence cracks of rock-like materials containing fissure-elliptical holes.

Fig. 15. Types of coalescence cracks of specimens containing different shapes of fissure-holes: (a) fissure-circular holes; (b) fissure-square holes.

Fig. 16. Stress distribution and crack growth process in rock-like materials containing fissure-elliptical holes with different ligament angles (i.e., 90°and 0°).

Fig. 17. Types of coalescence cracks of specimens containing fissure-elliptical holes with different ligament angles: (a) 90°; (b) 0°.

Fig. 18. Stress distribution and crack growth process in rock-like materials containing different combinations of fissure-holes: fissure-square hole and fissure-elliptical hole (CI); fissure-square hole and fissure-circular hole (CII); fissure-circular hole and fissure-elliptical hole (CIII).

Fig. 19. Types of coalescence cracks of specimens containing combinations of fissure-holes: (a) case CI; (b) case CII; (c) case CIII.

Table 1. Parameters applied in the simulations.

Materials	Parameters	Value
Solid elements	Density/kg·m^{-3}	2500
	Young's modulus/GPa	15
	Poisson's ratio	0.3
Steel plate	Density/kg·m^{-3}	7800
	Young's modulus/GPa	210
	Yield Strength/MPa	400
	Poisson's ratio	0.3
Cohesive elements	Initial shear stiffness/GPa·m^{-1}	5.28
	Initial tensile stiffness/GPa·m^{-1}	15
	Normal traction force/MPa	6
	Tangential traction force/MPa	22
	Model-I fracture energy/ N·mm^{-1}	0.06
	Model-II fracture energy/ N·mm^{-1}	0.165

Table 2. Schematics of fissure-holes in the numerical model.

Numerical number	α/°	R/mm	a/mm	b/mm	c/mm	S/mm^2	Geometric settings
AI	60	8	/	/	/	402.12	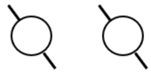
AII	60	/	/		14.18	402.12	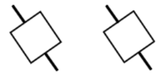
AIII	60	/	32	8	/	402.12	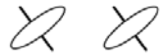
BI	90	/	32	8	/	402.12	
BII	0	/	32	8	/	402.12	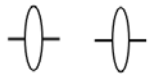
CI	60	/	32	8	14.18	402.12	
CII	60	8	/	/	14.18	402.12	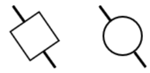
CIII	60	8	32	8	/	402.12	

Table 3. Coalescence modes of rock bridge between two fissure-holes.

Type	Image of coalescence pattern	Description of coalescence
DT	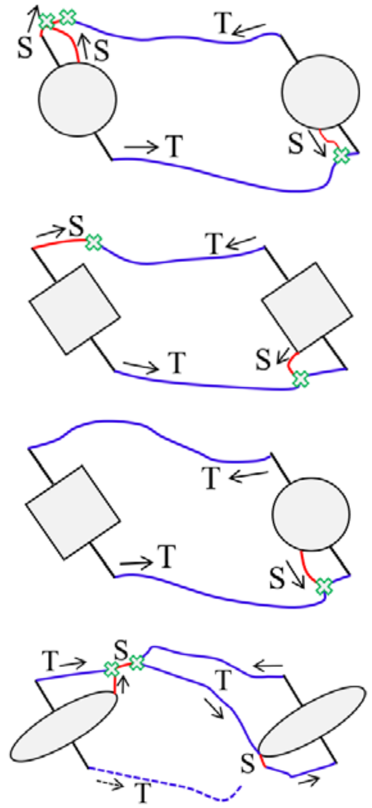	✧ The cohesive elements along the rock bridge coalescence cracks are dominated by tensile damage. Although shear damage occurs near the holes, the distribution is relatively limited. ✧ The crack junctions are mainly distributed near the fissure-holes. ✧ The coalescence patterns consist of two principal paths. ✧ The mode "DT" is prone to occur when the ligament angle of the fissure-hole is 60° in this paper. Please note: The symbol of → represents the direction of crack propagation; The T means the tensile crack, and S means the shear crack. × means the crack junction; The dashed line respects the un-coalescence cracks, while the solid line means the coalescence cracks.
T	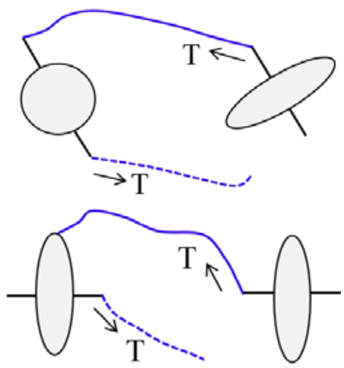	✧ The cohesive elements along the rock bridge coalescence cracks are only caused by tensile damage. ✧ No crack junction appears. ✧ The coalescence pattern consists of one principal path. ✧ The mode "T" is prone to occur when the ligament angle of the fissure-hole is no higher than 60° in this paper.
S+T	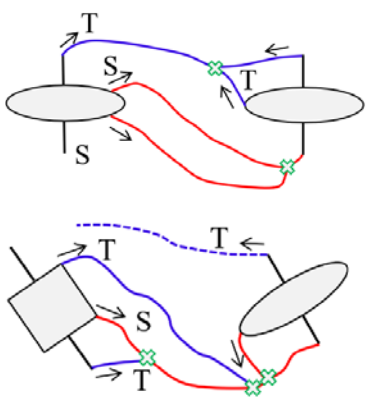	✧ The cohesive elements along the rock bridge coalescence cracks are caused by not only tensile damage but also shear damage. ✧ The crack junctions are mainly distributed near the right fissure-hole. ✧ The coalescence pattern consists of four principal paths. ✧ The mode "S+T" is prone to occur when the ligament angle of the fissure-hole is no less than 60°in this paper.

DT: Dominated by tensile damage, T: Tensile damage, S+T: shear and tensile damage

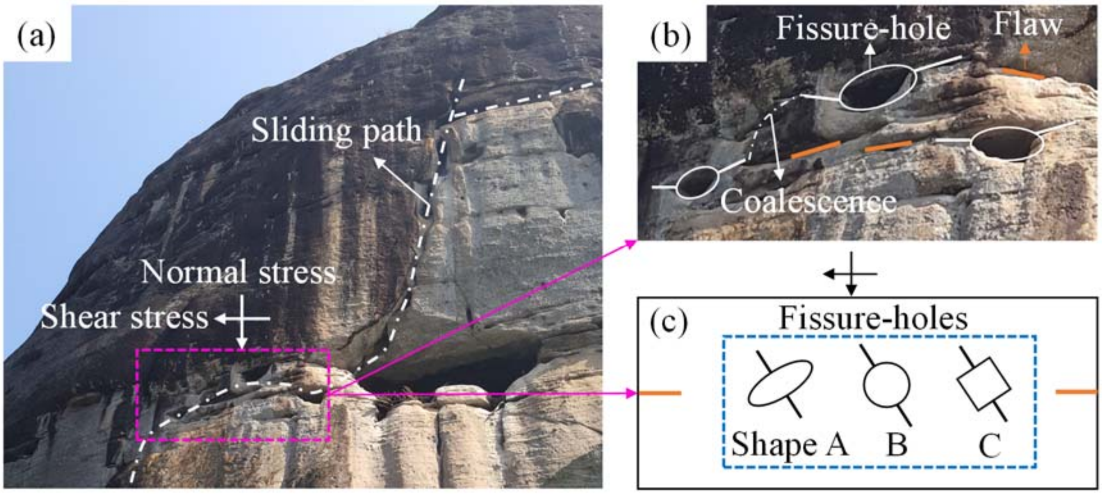

Fig.1. Rock mass high slopes: (a) potential sliding path of rock mass containing fissure-holes (Chongqing, China); (b) detailed descriptions of fissure-holes; (c) shapes of fissure-holes considered in this paper.

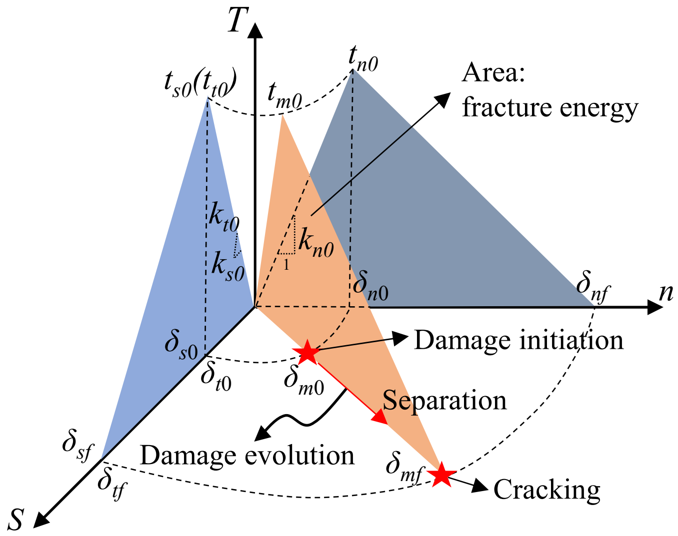

Fig.2. Mixed-mode traction-separation response.

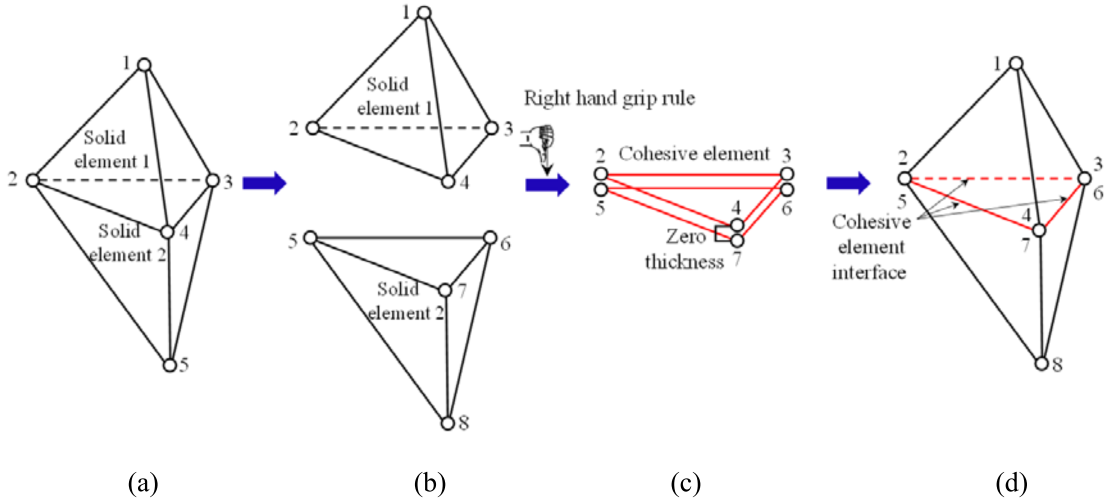

Fig. 3. Inserting a zero-thickness cohesive element between solid elements: (a) two adjacent solid elements; (b) re-arranged nodes of solid elements; (c) zero-thickness cohesive element (COH3D6); (d) insertion of a cohesive element.

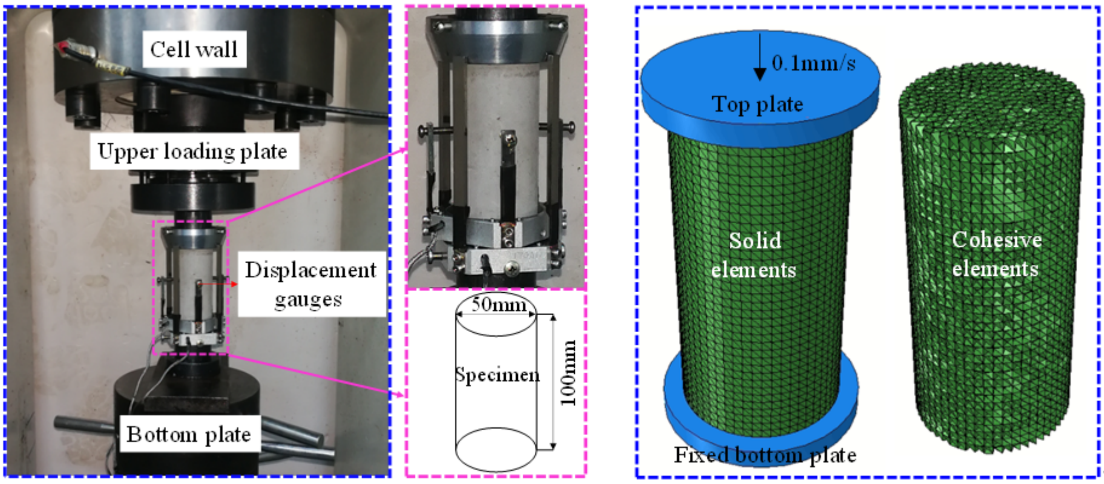

(a) (b)

Fig.4. Uniaxial compression test: (a) Laboratory test; (b) numerical model.

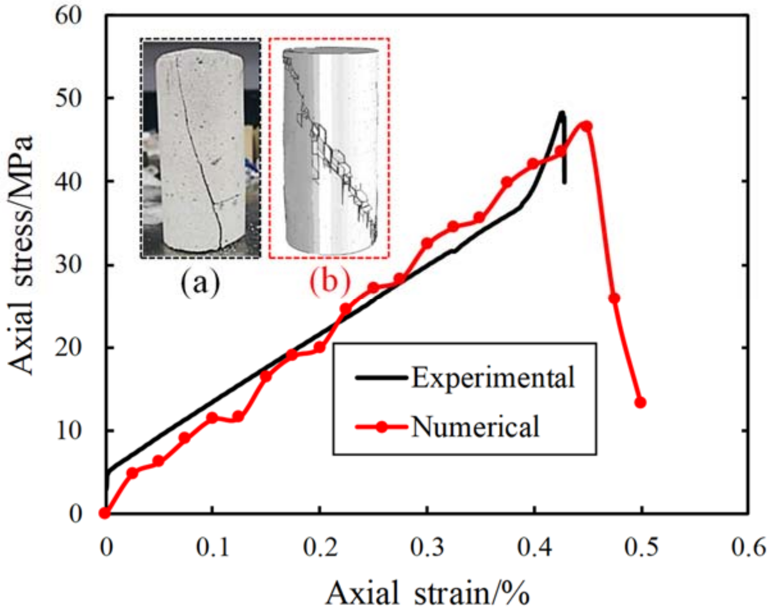

Fig.5. Comparison of experimental and numerical results in the uniaxial compression test.

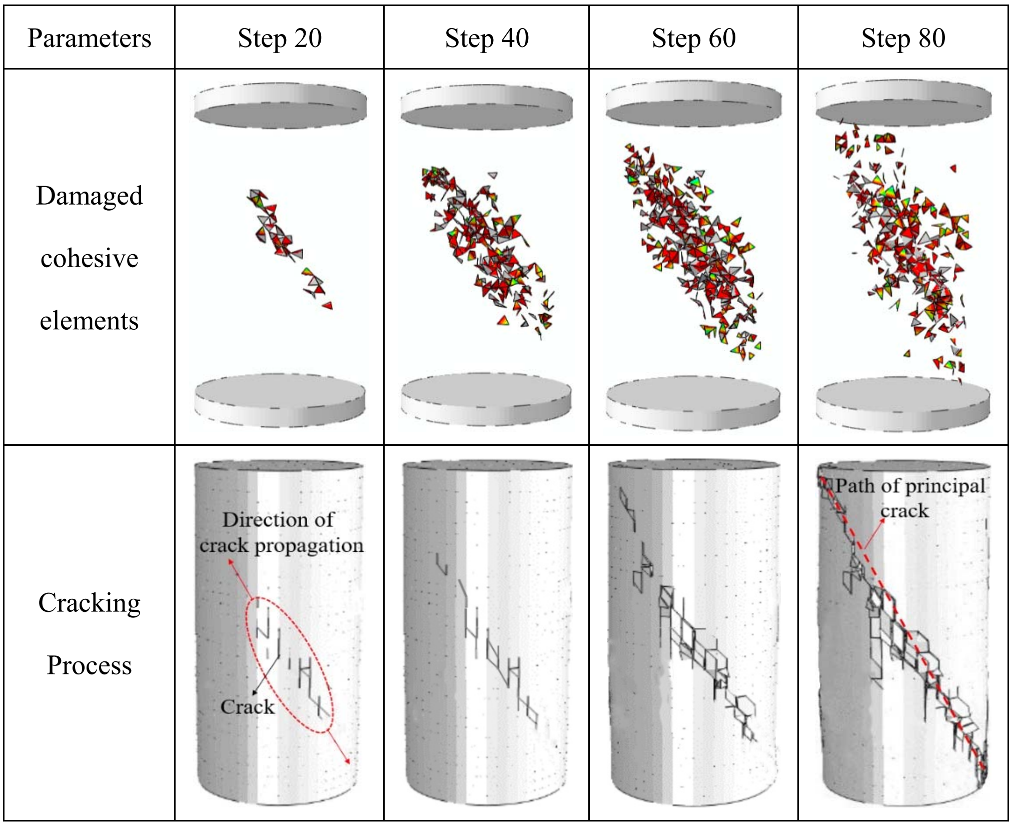

Fig.6. Fracture process of the specimen under different steps.

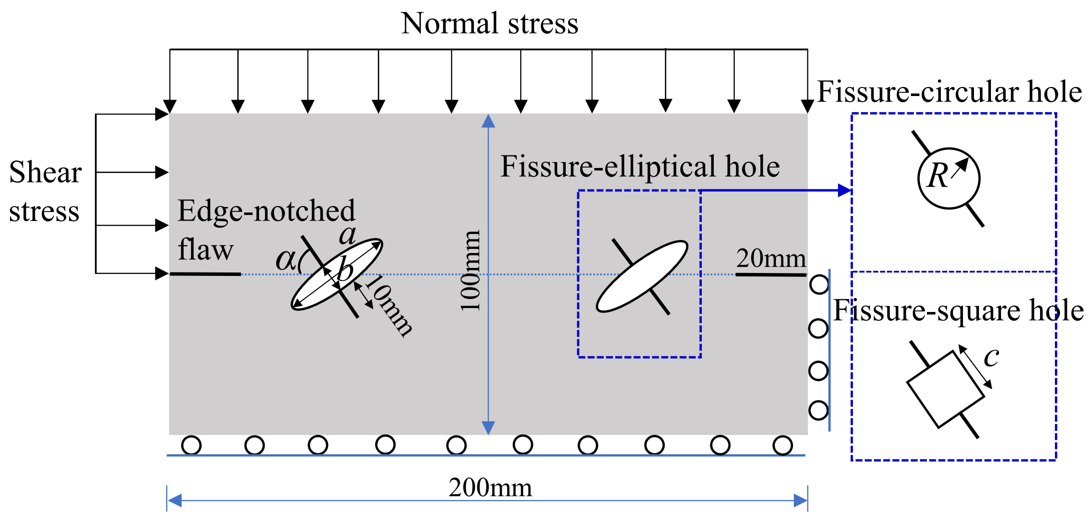

Fig. 7. A conceptual model for rock-like materials containing fissure-holes under the shearing effect.

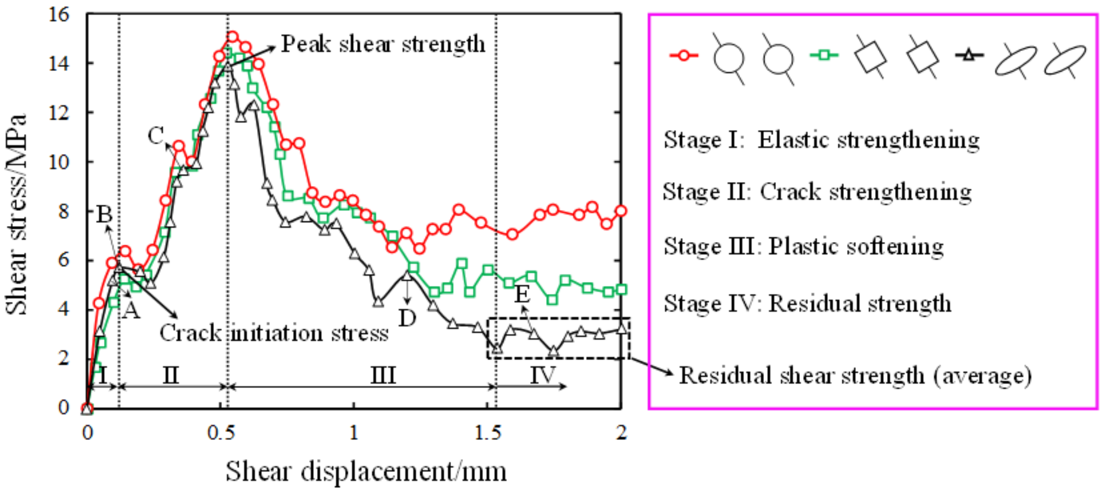

(a)

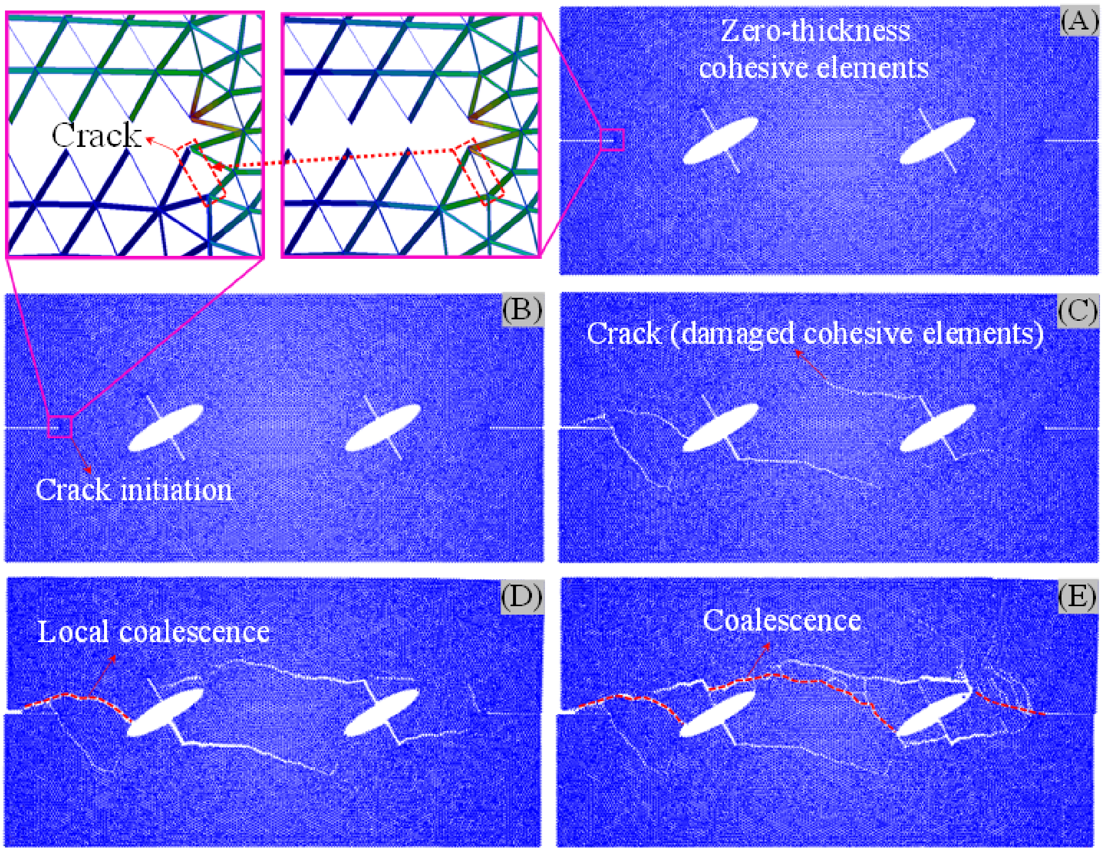

Fig.8. Shearing process of rock-like materials containing fissure-hole flaws: (a) shear stress-shear displacement curves under different shapes of fissure-holes; (b) characteristics of cohesive elements.

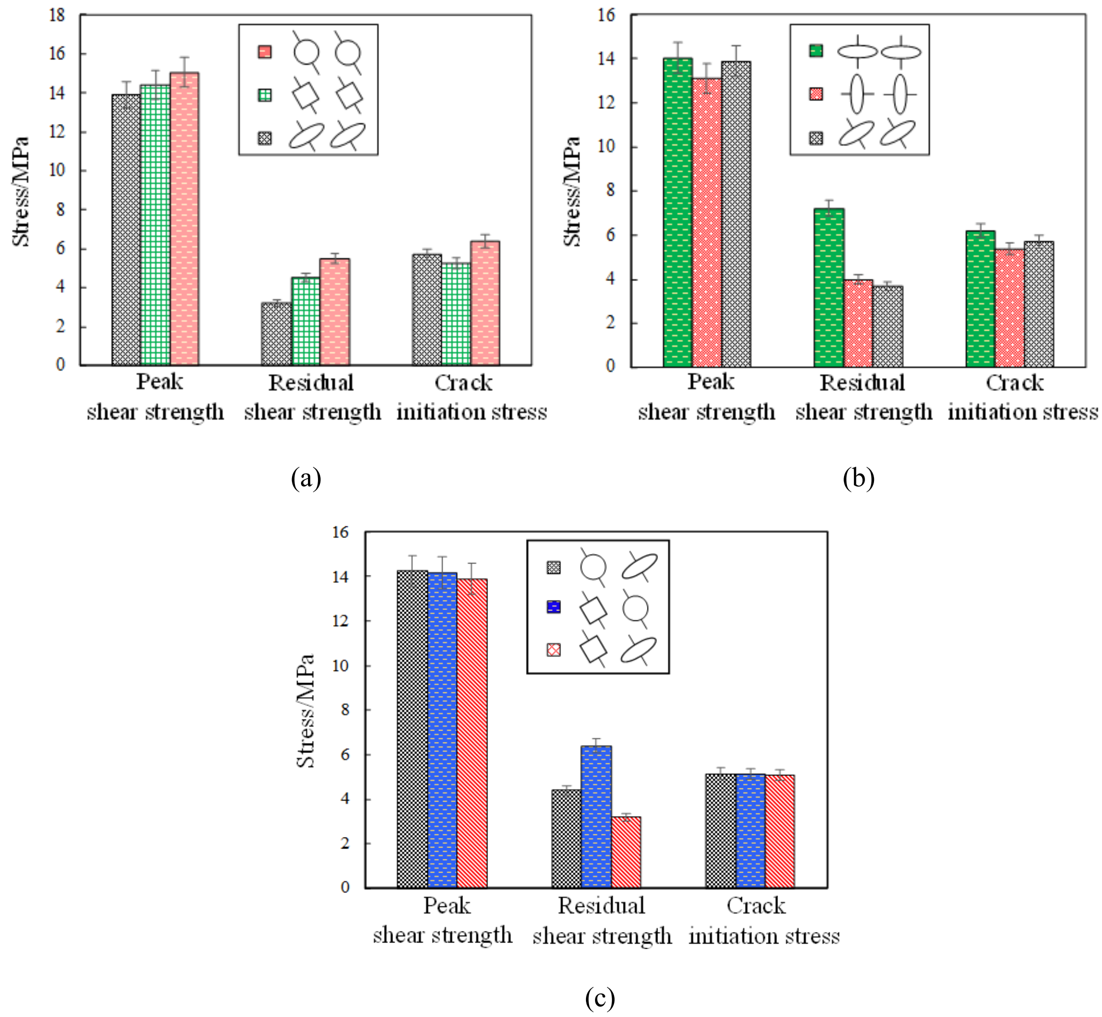

Fig.9. Mechanical properties (i.e., peak shear strength, residual shear strength, and crack initiation stress) of rock-like materials containing fissure-holes: (a) different shapes of fissure-holes; (b) different ligament angles of fissure-holes; (c) different combinations of fissure-holes.

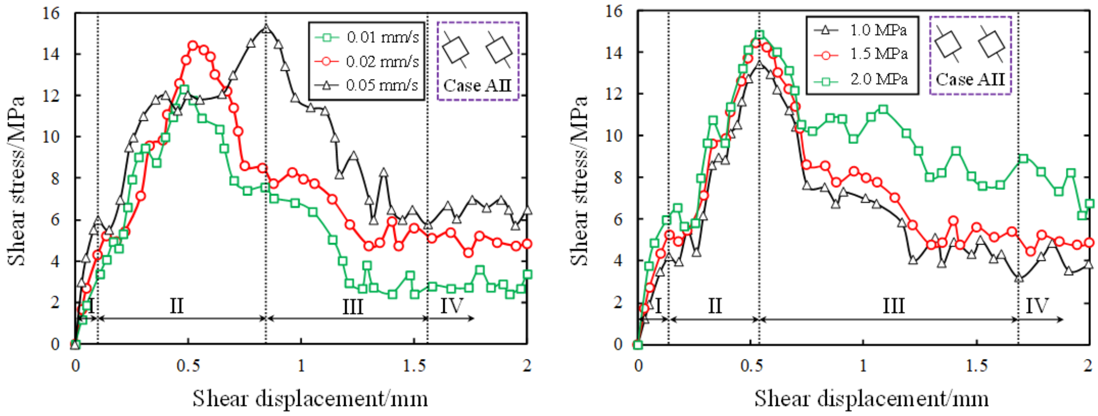

(a) (b)

Fig. 10. Curves of shear stress-shear displacement under different loading conditions: (a) different shear rates; (b) different applied normal stress levels.

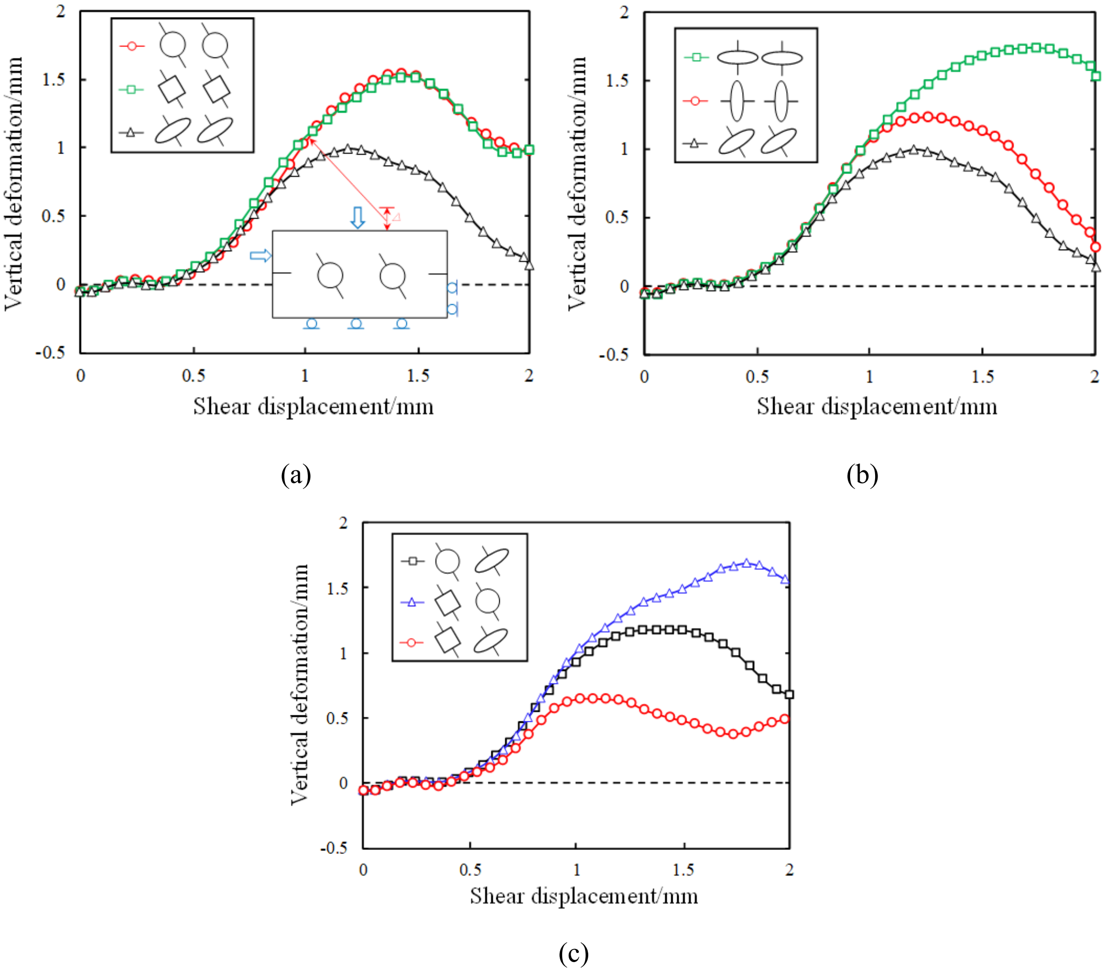

Fig.11. Curves of vertical deformation-shear displacement: (a) different shapes of fissure-holes; (b) different ligament angles of fissure-holes; (c) different combinations of fissure-holes.

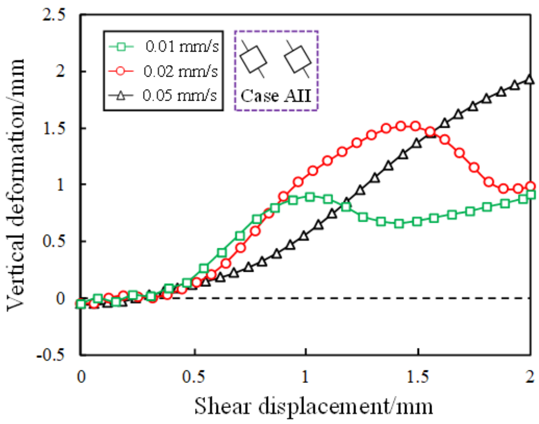

(a)

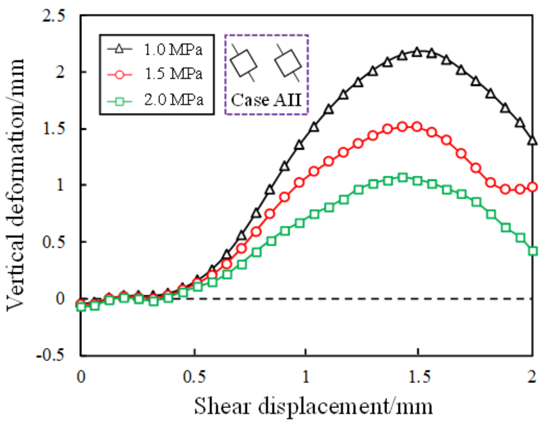

(b)

Fig.12. Curves of vertical deformation-shear displacement of rock-like materials containing fissure-holes under different loading conditions: (a) different shear rates; (b) different applied normal stress levels.

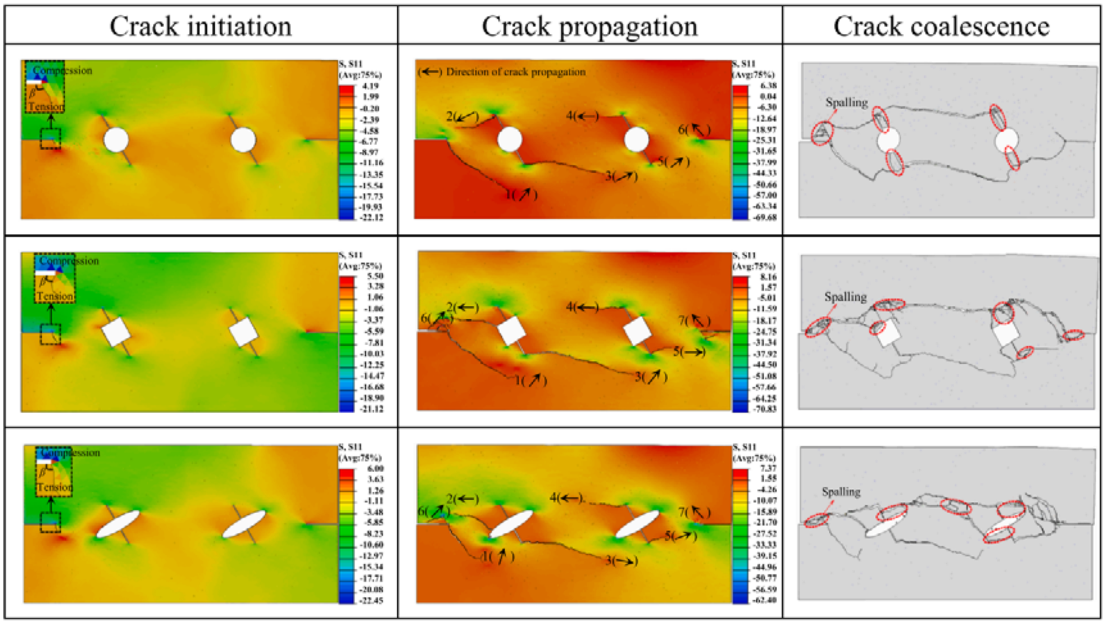

Fig. 13. Stress distribution and crack growth process in rock-like materials containing different shapes of fissure-holes (i.e., fissure-circular holes, fissure-square holes, and fissure-elliptical holes).

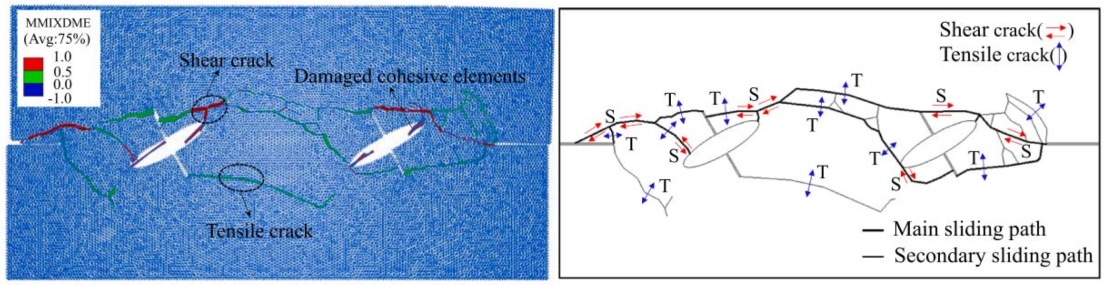

(a) (b)

Fig. 14. Shear failure pattern: (a) types of damaged cohesive elements; (b) coalescence cracks of rock-like materials containing fissure-elliptical holes.

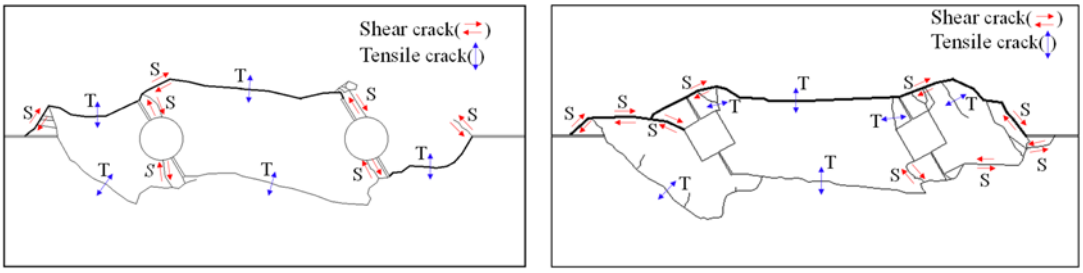

(a) (b)

Fig.15. Types of coalescence cracks of specimens containing different shapes of fissure-holes: (a) fissure-circular holes; (b) fissure-square holes.

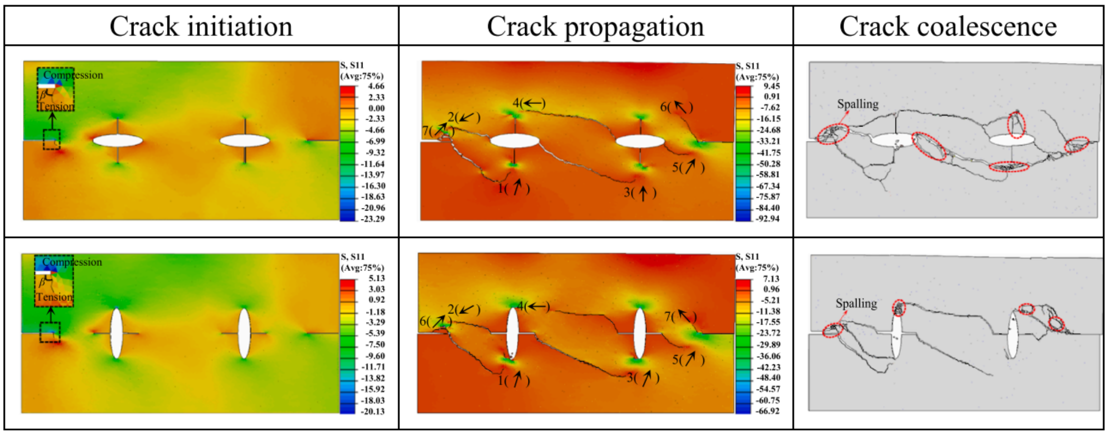

Fig. 16. Stress distribution and crack growth process in rock-like materials containing fissure-elliptical holes with different ligament angles (i.e., 90°and 0°).

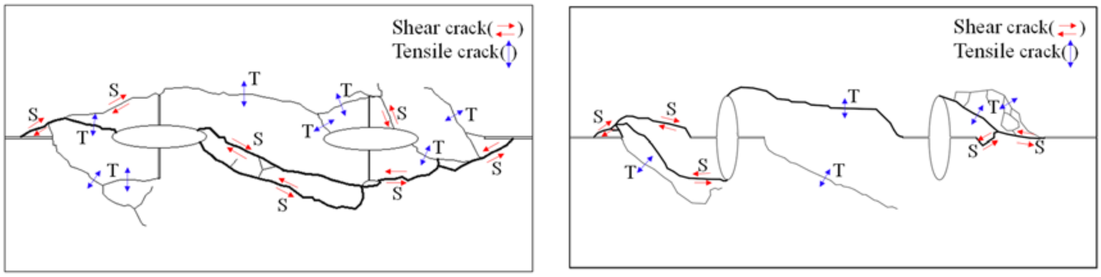

(a) (b)

Fig.17. Types of coalescence cracks of specimens containing fissure-elliptical holes with different ligament angles: (a) 90°; (b) 0°.

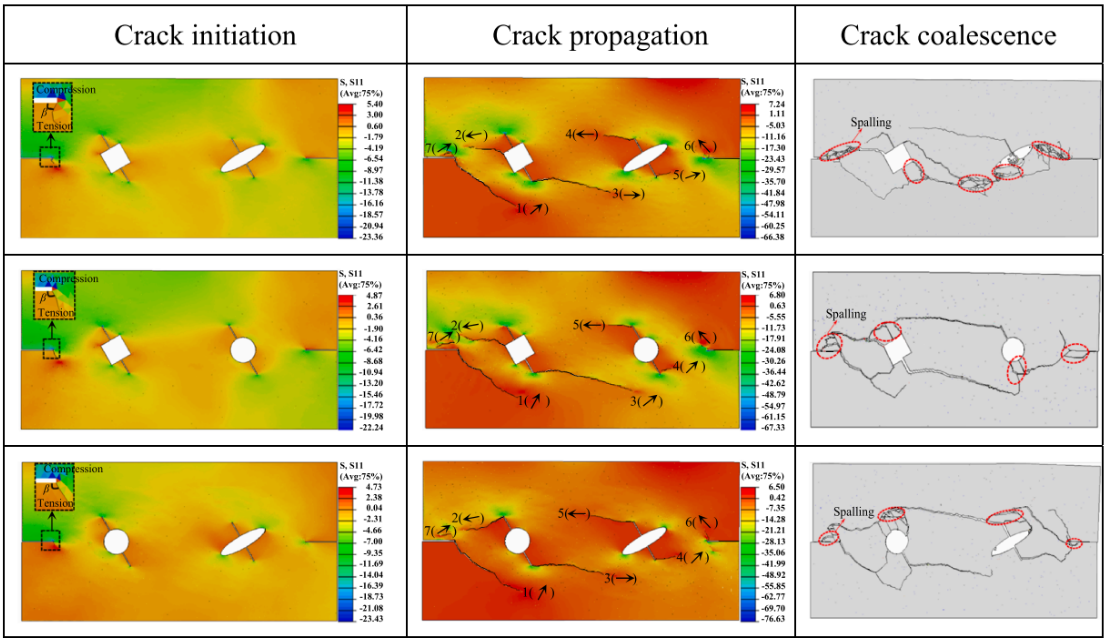

Fig.18. Stress distribution and crack growth process in rock-like materials containing different combinations of fissure-holes: fissure-square hole and fissure-elliptical hole (CI); fissure-square hole and fissure-circular hole (CII); fissure-circular hole and fissure-elliptical hole (CIII).

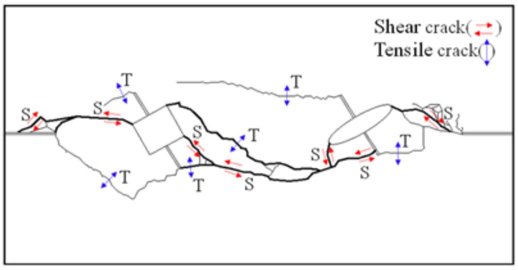

(a)

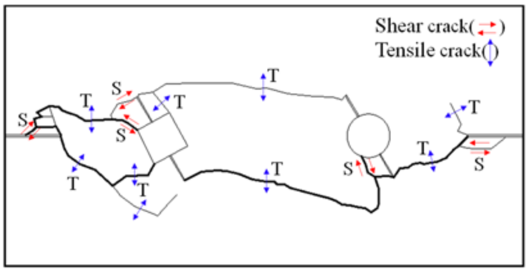

(b)

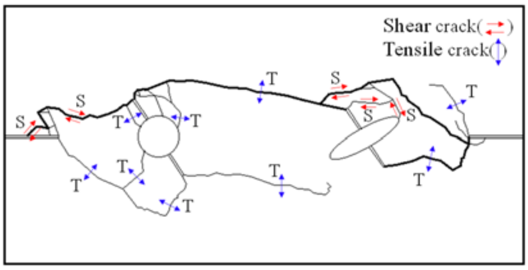

(c)

Fig. 19. Types of coalescence cracks of specimens containing combinations of fissure-holes: (a) case CI; (b) case CII; (c) case CIII.